Towards a Unified Fold-Cusp Model for Bond Polarity Scaling: Electron Rearrangements in the Pyrolytic Isomerization of Cubane to Cyclooctatetraene

Leandro Ayarde-Henríquez,[1*] Cristian Guerra,[2*] and Eduardo Chamorro[3*]

[1]Trinity College Dublin. School of Physics, Dublin 2, Ireland. AMBER, Advanced Materials and BioEngineering Research Centre, Dublin 2, D02 CP49, Ireland. Corresponding Author (L Ayarde-Henríquez). E–mail: leandro.ayarde@tcd.ie ORCID ID: https://orcid.org/0000–0001–5963–6028.

[2]Universidad Autónoma de Chile. Facultad de Ingeniería. Avenida Pedro de Valdivia 425, 7500912, Santiago de Chile. Chile; Universidad de Córdoba. Grupo de Química Computacional. Facultad de Ciencias Básicas. Carrera 6 No. 77-305, Montería-Córdoba, Colombia. Corresponding Author (C. Guerra). E-mail: xguerracbn@gmail.com. ORCID-ID: https://orcid.org/0000-0002-9664-2504.

[3]Universidad SEK Chile. Instituto de Investigación Interdisciplinar en Ciencias Biomédicas (I3CBSEK). Santa María 0760, Providencia, Santiago, Chile. Corresponding Author (E. Chamorro). E-mail: ed.chamorro9@gmail.com. ORCID-ID: https://orcid.org/0000-0002-9200-9859.

Abstract

This study meticulously examines the criteria for assigning electron rearrangements along the intrinsic reaction coordinate (IRC) leading to bond formation and breaking processes during the pyrolytic isomerization of cubane (CUB) to 1,3,5,7-cyclooctatetraene (COT) from both thermochemical and bonding perspectives. The computed gas-phase activation enthalpies obtained using state-of-the-art DFT functionals strongly align with experimental values. Notably, no cusp-type function was detected in the initial thermal conversion step of CUB to bicyclo[4.2.0]octa-2,4,7-triene (BOT), as evidenced by examining the modulus of the Hessian determinant at all potentially degenerate critical points (CPs) and their relative distances. Contrary to previous reports, all relevant fluxes of the pairing density must be described in terms of fold unfolding. The transannular ring opening in the second step highlights characteristics indicative of a cusp-type catastrophe, facilitating a direct comparison with fold features. This fact underscores the critical role of density symmetry persistence near topographical events in determining the type of bifurcation. A fold-cusp unified model for scaling the polarity of chemical bonds is proposed, integrating ubiquitous reaction classes such as isomerization, bimolecular nucleophilic substitution, and cycloaddition. The analysis reveals that bond polarity index (BPI) values within the $[0, 10^{-5}]$ au interval correlate with cusp unfolding, whereas fold spans over a broader $[10^{-3}, \infty)$ au spectrum. These insights emphasize that the cusp polynomial is suitable for describing chemical processes involving symmetric electron density distributions, particularly those involving homolytic bond cleavages; in contrast, fold characterizes most chemical events. The elucidated unified model accurately captures the CUB to COT stepwise reaction mechanism, as illustrated by the sequence of catastrophes describing ELF topology changes along the IRC. The rigorous application of BET and identifying unfoldings that describe crucial electron rearrangements are highlighted as essential for understanding and predicting chemical reactivity.
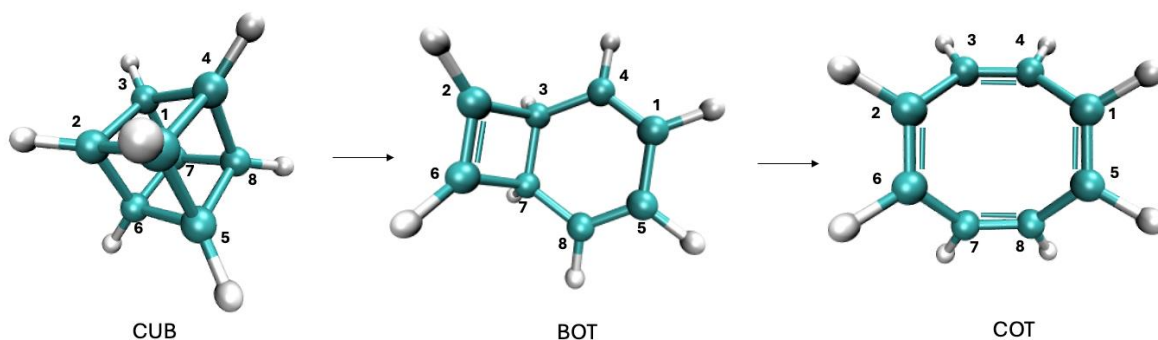
Keywords Bonding Evolution Theory (BET); Gas-phase thermochemistry; Catastrophe Theory; Annulenes thermal isomerization; Hessian matrix; Electron density symmetry

We dedicate this paper to Professor Alejandro Toro-Labbé. His unwavering support, mentorship, and pioneering research have influenced our work. This paper is part of the special collection celebrating his 70th birthday, honoring his legacy and impact on the scientific community.

1

1. Introduction

Chemists have been fascinated by the molecular structure and physical properties of cubane (CUB) and its derivatives for almost six decades [1-11]. The cubic symmetry and extreme bond strain of cubane result in unique chemical behaviors that continue to challenge and inspire synthetic chemists[12-14]. The rigid C8 framework, characterized by bond angles of 90°, defies the typical tetrahedral geometry associated with sp³ hybridized carbon atoms, leading to significant angular strain and high strain energy [7, 12, 15]. This strain is a driving force behind the distinctive reactivity of cubane [16], often facilitating reaction pathways that are less accessible in less strained systems [5, 13]. Additionally, the geometric rigidity of cubane ensures that introducing substituents at any of its eight carbon atoms results in well-defined and predictable structural modifications [11-14]. This fact makes cubane an excellent scaffold for the design of new materials and pharmaceutical compounds [14], where its compact, energy-dense nature can be harnessed to create molecules with novel properties, such as enhanced stability, specific steric interactions, and the ability to store and release significant amounts of energy in controlled environments [2, 13, 17, 18]. The exploration of cubane derivatives has already led to advances in developing high-energy materials, pharmaceuticals, and even molecular machines, highlighting this remarkable framework's ongoing relevance and clear potential in modern chemistry [3, 4, 6, 8-10].

The inherent strain and distinctive geometric features of cubane have sparked interest in its synthesis and stability and prompted further exploration into its reactivity and transformation pathways [12-14]. Indeed, cubane is an excellent model system for theoretical studies, strain energy analysis, and reactivity [19]. Investigating bond dissociation energies and the nature of chemical bonding in cubane provides valuable insights into strained molecules. One of the significant model transformations is the thermal decomposition of CUB to cyclooctatetraene (COT) [20]. This process highlights the dynamic interplay between the structural strain and the resulting thermochemical properties as modeling the conversion towards more stable isomers [5, 13, 19, 20]. Recently, Seif and co-workers [21] have presented computational results concerning such a thermal decomposition via a two-step mechanism involving the formation of bicyclo[2.2.2]octane (BOT) as an intermediate, as illustrated in **Scheme 1**.

Scheme 1. Thermal decomposition of cubane (CUB) to yield cyclooctatetraene (COT) via the intermediate bicyclo[2.2.2]ocane (BOT) [21].

Based on the application of bonding evolution theory [22], they provide evidence that supports bond-breaking/bond-forming processes and the associated electron density rearrangements to be asynchronous along the entire reaction path. The reaction mechanism features thus 18 structural stability domains (SSDs) separated by 17 bifurcation catastrophes of fold and cusp nature, specifically denoted [23] as η-1-13-C†C†FFFC†C†FFFC†C†-2-6-[C]$_2$C†[F]$_2$[C†]$_2$C†-0 [20]. *Considering recent findings regarding the characterization of such processes involving CC bonding [24], this observation warrants a more detailed examination. Cusp-type catastrophes are particularly significant, as they are typically anticipated only in cases where local symmetry is preserved throughout the reactive process [24-35].*

Within the BET framework, a reacting system is modeled as a gradient dynamical system (GDS), with the electron localization function (ELF) [36] as the time-independent "potential function" [37]. BET uses catastrophe theory principles to characterize sudden changes in ELF along the reaction coordinate. Let us briefly outline the basis of CT [38], as comprehensive resources are readily available [37-40]. The gradient nullity condition applied to the smooth $\mathbb{R}^3$ ELF potential results in four types of equilibrium or critical points (CPs): attractors of index zero (local maxima), saddles of index one and two, and repellors of index three (local minima). The index stands simply for the number of positive eigenvalues of the Hessian matrix evaluated at the CP. The collection of CPs defines the molecular map or phase-space portrait of the gradient vector field of the examined local potential [41, 42]. The curvature of the phase space flattens as the distance between two or more critical points (CPs) decreases. This change in curvature can be directly evaluated using the determinant of the Hessian matrix, |det H|. A CP is termed degenerate if the |det H| evaluated at this point yields a zero value [39, 40, 43]. *Catastrophe theory describes all distinct changes in the geometric shape of generic parametric families triggered by the creation or annihilation of CPs through seven unfoldings, constrained to a maximum of four parameters, provided these CPs are not exclusively saddle points [39]. This observation underscores that merely counting changes in the number and type of Morse critical points separating adjacent structurally stable domains (SSDs) is insufficient for determining the associated parametric unfolding [24-35].* BET provides a chemically convenient perspective[44-51] on the behavior of dynamical systems by examining bifurcations that occur due to changes in the gradient field of a well-characterized local function along a given reaction coordinate. ELF is a *local* function describing the relative electron pair (de)localization associated with a given electron density [52-54]. ELF can be understood as the relative local excess of kinetic energy density resulting from the Pauli exclusion principle [36, 44, 50, 52-55]. Integrating the one-electron and two-electron density probabilities within the volume of ELF basins makes it possible to assess electron delocalization quantitatively [36, 44, 52-58]. Sudden variations in the number and type of critical points (CPs) along the reaction path can be associated with relevant electronic events responsible for bond-breaking and bond-forming processes. Based on Thom's theorems [39, 59-61], this link is established via the so-called universal unfoldings [38]. The system evolution is sketched into a sequential series of structural stability domains (SSDs) defined by a definite number and type of nondegenerate critical points of the gradient field of ELF [22, 62-66]. Each SSD can, in principle, be associated with a given "bonding state" of the evolving system [24-35]. The turning points separating each pair of SSDs can be properly associated with the results of discontinuities or elemental bifurcation catastrophes [22, 61, 64]. This comprehensive understanding of SSDs and their bifurcation points provides a rigorous framework for analyzing the reaction mechanism and bridges theoretical models with practical chemical intuition. The BET approach has provided significant

3

insights into the fundamental mechanisms of chemical reactions, as evidenced by examining different bonding challenges [67]. *Recent advancements in the rigorous application of the BET methodology have evidenced that describing relevant chemical events along a reactive coordinate of only visually inspecting the sudden changes in the number and type of critical points leads to erroneous assigning of the unfolding characterizing electronic rearrangements* [29]. It is crucial to assess local curvature metrics involving the Hessian matrix at potentially degenerate CPs and to monitor the distance variation between them to avoid misinterpretations. Building on the ongoing interest in the detailed study of bifurcations in ELF topology along reaction coordinates [24-35], our approach employs a methodological framework that assesses the modulus of the Hessian matrix determinant, |det H|, evaluated at all potentially degenerate critical points (CPs) of the ELF, the relative distance between these CPs, and the maximum number of CPs associated with each unfolding [24-35]. As we will discuss, a notable and striking finding emerges, significantly diverging from previous cubane pyrolysis observations [21]. These results will highlight the complex interrelationships between the minimal energetic configurations of the reaction system, key electron reorganizations, and the associated topological changes. We aim to demonstrate that identifying key fluxes of electric charge along a reaction path is far more than a technical detail; it is pivotal in utilizing Thom's polynomials as effective markers of the persistency of electron-pairing densities [33, 35]. Henceforth, such a comprehensive approach to analyzing chemical reactions addresses the intricacies of electronic rearrangements and offers an opportunity to provide a deeper understanding of bond polarity intimately related to the electronegativity concept [68, 69]. Metrics associated with the bond polarity index (BPI), as originally proposed by Allen and co-workers [70, 71] can be utilized to assess bond polarity, providing new insights into the chemical implications rationalizing previous findings [24-35]. This work is organized as follows: First, we briefly outline the theoretical foundations of BET and describe the computational methodologies employed. Next, we provide a detailed re-evaluation of the topographic aspects of the thermal conversion mechanism from cubane (CUB) to cyclooctatetraene (COT). We then introduce a bond polarity scale based on the fold-cusp composite model, utilizing the connection between universal unfoldings and the symmetry of electron density in bond-breaking and bond-forming regions. The last section summarizes the main findings.

2. Theoretical and computational details

Geometry optimization using analytical gradients [72-75], frequency calculations, and the assessment of thermochemical properties regarding the pyrolytic isomerization of CUB to BOT were performed using the B3LYP hybrid functional in combination with both the 6-31G(d) and 6-31+G(d,p) Pople basis sets. All calculations concerning thermal conversion from BOT to COT were tested with the B3LYP, ωB97X-D, M06-2X, and MN15-L functionals, each combined with the 6-31+G(d,p) split-valence basis set, as implemented in the Gaussian 16 package of programs [76]. The intrinsic reaction coordinate (IRC) [77, 78] was obtained for both chemical reactions using the standard integration method [74, 75] with a step size equal to 0.001 amu$^{1/2}$Bohr to validate that the transition structure connected the correct minima.

The topological analysis of the ELF and the characterization of its phase-space portrait were carried out using the Multiwfn package of programs [79]. The topographic maps were generated using the VMD software [80]. The fulfillment of the Poincaré-Hopf relationship was verified for all topographic maps along the IRC. The classification of topographical bifurcations was carried out by
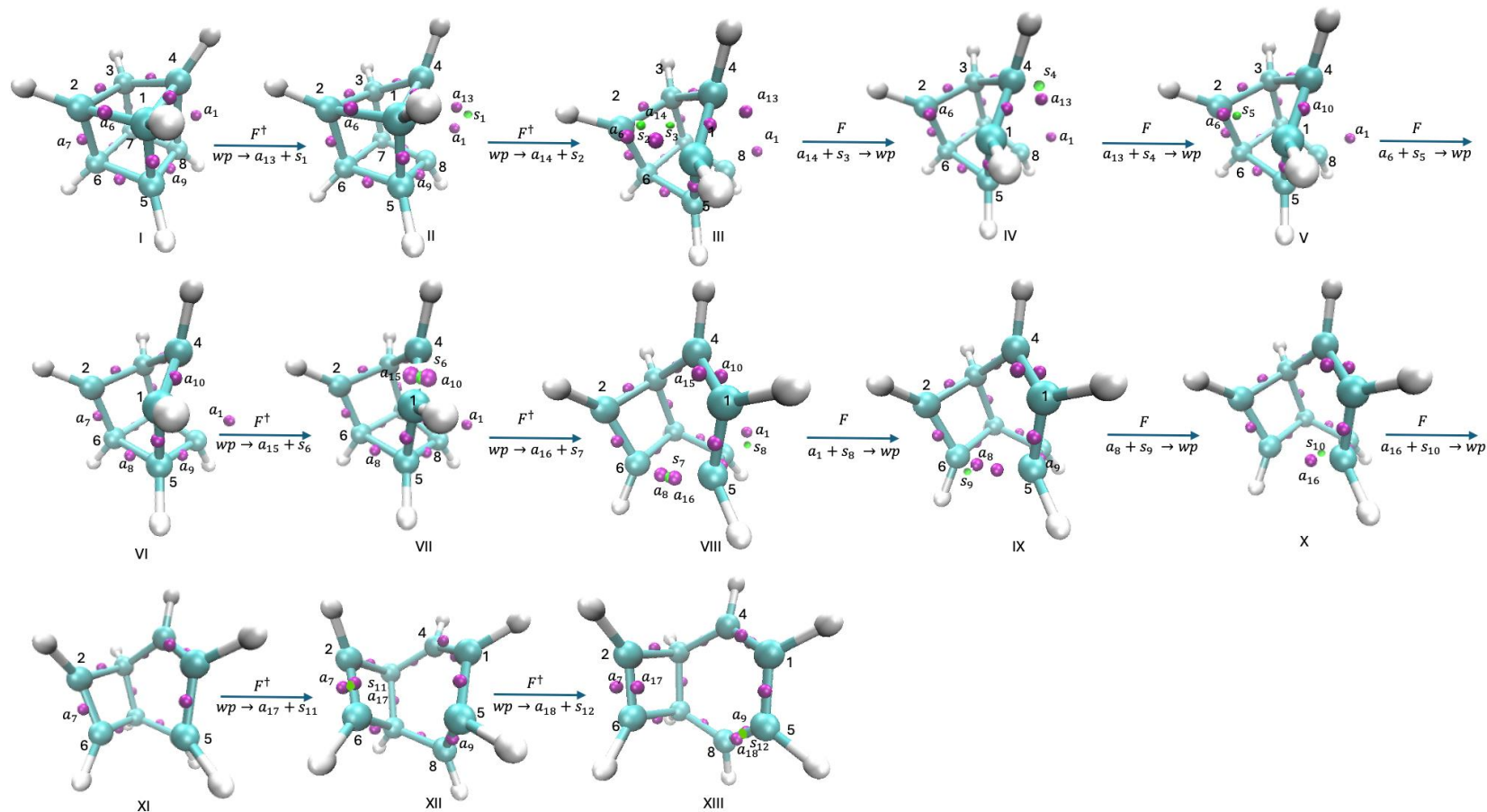
4

strictly examining the *absolute value of the Hessian determinant evaluated* at *all potentially degenerate critical points and their relative distance* near the degeneration region. To elucidate the nature of elementary catastrophes associated with bond-breaking and bond-forming processes, we employ a three-step sequential procedure [29] based on the CT principles [22, 23, 63-65, 81-84]. This method enables the accurate identification and assignment of the correct unfolding, i.e., first, the determinant of the Hessian matrix is evaluated at all potentially degenerate critical points, excluding cases where all points are saddle points. Second, the relative distance between potentially degenerate critical points is evaluated, again excluding cases with only saddle points. This step is instrumental when the potential energy surface is relatively flat. Finally, the unfolding assignment process relies on the outcomes of the first two steps, considering the maximum number of critical points for each universal unfolding [29]. The BPI has been evaluated [79] following the metric proposed by Allen and coworkers [70, 71], i.e., $BPI_{XY} = \left(EI_X - EI_X^{Ref}\right) - \left(EI_Y - EI_Y^{Ref}\right)$, where EI_X^{Ref} and EI_Y^{Ref} are the energy index of the reference system for atoms X and Y, respectively. A larger magnitude of BPI_{XY} indicates a higher bond polarity of the X-Y bond. It is worth mentioning that $EI_X = \sum_i^{valence} n_i \varepsilon_i \sigma_{i,X} / \sum_i^{valence} n_i \sigma_{i,X}$, where $\sigma_{i,X}$ is a matrix representation for atom X in the i-th molecular orbital, with occupation n_i and energy ε_i. Diffuse functions were avoided in such a context, as we use the simple Mulliken-based population partition for obtaining $\sigma_{i,X}$. Despite EI and BPI being essentially one-electron measures [70, 71, 85, 86], has been demonstrated to be functional parameters in predicting the behavior of chemical bonds along related series of molecules and materials-related complex systems [87-89].

3. Results and Discussion

3.1. Thermal cage-opening process of cubane.

To our knowledge, there is no record of an experimental barrier for the $CUB \rightarrow BOT$ reaction. Nonetheless, static pyrolytic experiments performed in the 503.15-533.15 K range report an activation energy of 43.0 kcal/mol for the cage-opening pathway leading to syn-tricyclo[4.2.0.0^{2,5}]octa-3,7-diene, which is 39.0 kcal/mol above COT [90]. Predicted activation enthalpies $\Delta H^{\ddagger}$ in the gas phase, computed using the popular B3LYP exchange-correlation functional combined with the 6-31G(d) and 6-31G+(d,p) split-valence basis sets, are consistent with the experimental measurements [90, 91]. This suggests that the level of theory used is appropriate for examining the ELF topography along the IRC and the invariance of results concerning the level of theory, corroborating previous observations [24, 46, 92, 93]. Hereafter, the provided distance values between reacting centers correspond to the B3LYP/6-31G(d) level. In **Scheme 2**, we report molecular graphs associated with all identified structural stability domains of ELF, namely SSDs labeled from I to XIII. All identified catastrophes are classified as the fold type involving one maximum and one index-one saddle, and in contrast to the previous assignations [21], no signatures for cusp types have been found. It is worth noting that the fold is the simplest unfolding, i.e., it is a third-degree polynomial characterized by one state variable and one control parameter. In contrast, the cusp is a fourth-degree function with two control parameters. The first two topological ELF bifurcations, $SSD\ I \rightarrow SSD\ II \rightarrow SSD\ III$, correspond to the C4-C8 and C1-C2 bond breakings, which are associated with a_1 and a_6 maximums, respectively. Seif and co-workers [21] characterized both events

5

through cusp-type functions, meaning that a_1 and a_6 degenerate and split into three hyperbolic CPs: two maxima and an index-one saddle point. However, a deeper examination [29] reveals an entirely different result. By following the absolute determinant of the Hessian matrix, |det H|, at maxima a_1 and a_6, any signature for degeneration can be found. Conversely, the |det H| increases towards more positive values in the neighborhood of the topographical bifurcation (see Supporting information, Fig S1). The number of CPs for each event varies in two, and neither a_1 nor a_6 are involved. Specifically, once the C4-C8 length reaches a value of 2.269 Å, the maximum a_{13} and the saddle s_1 originate near the C4 carbon from a wandering point (wp), i.e., $wp \rightarrow a_{13} + s_1$, whereas the maximum a_1 remains near the C8 center. This change in the ELF phase portrait constitutes the onset of the C4-C8 breaking. As the reaction evolves, and the C1-C2 distance is 2.011 Å, another fold process, i.e., $wp \rightarrow a_{14} + s_2$ occurs in the locality of the C1 center, marking the initial stages of the C1-C2 cleavage, whereas the maximum a_6 remains as a non-degenerated CP near the C2 center. Hence, these CC bond breakings should be described as the simplest unfolding, i.e., the fold. Note that regardless of the inherent complexities of the above cage- and ring-opening events, which are influenced by a variety of factors, including the activation enthalpy, species concentration, partial and total pressure, temperature, molar mass, heat capacities, and steric effects, both topological changes can be studied via the universal unfolding expression $\eta(r, \mu) = x^3 + \mu x \pm y^3$, where η is the ELF, x stands for the state variable (i.e., the eigenvector associated with the vanishing eigenvalue), y designates any arbitrarily orthogonal degree of freedom with respect to x, and μ is the control parameter. This parameter is conveniently (yet arbitrarily) defined as the negative in the length variation of reaction centers, yielding real roots (i.e., CPs) [29]. Considering recent discussions [24-35], it becomes clear that assigning a cusp function to bond-breaking processes implies that the electron pairing density (indicative of a bond) splits into two equivalent fractions. The homolytic bond dissociation of molecular systems resulting in two identical moieties, each bearing an unpaired electron (in the case of closed-shell systems), accurately exemplifies this situation [29]. In contrast, the |det H| evaluated at a_1 and at a_6 reveals an entirely different picture concerning the cage-opening and ring-opening, respectively. The density represented through such ELF maxima does not split. An essential element in the current discussion is the analysis of CUB geometric changes along the IRC.

Scheme 2. Simplified molecular structures, critical points, and topology changes connecting the different structural stability domains (SSDs, labeled using Roman numbers), which feature bonding states associated with the CUB cage-opening process. Violet numbered spheres represent ELF maxima, and green numbered spheres are saddles of index one. The CUB, the transition state (TS), and BOT species belong to SSDs I, V, and XIII, respectively. The labels $F^\dagger$ or F represent fold bifurcations that increase or decrease the number of basins, respectively, as summarized by the process below the arrow.
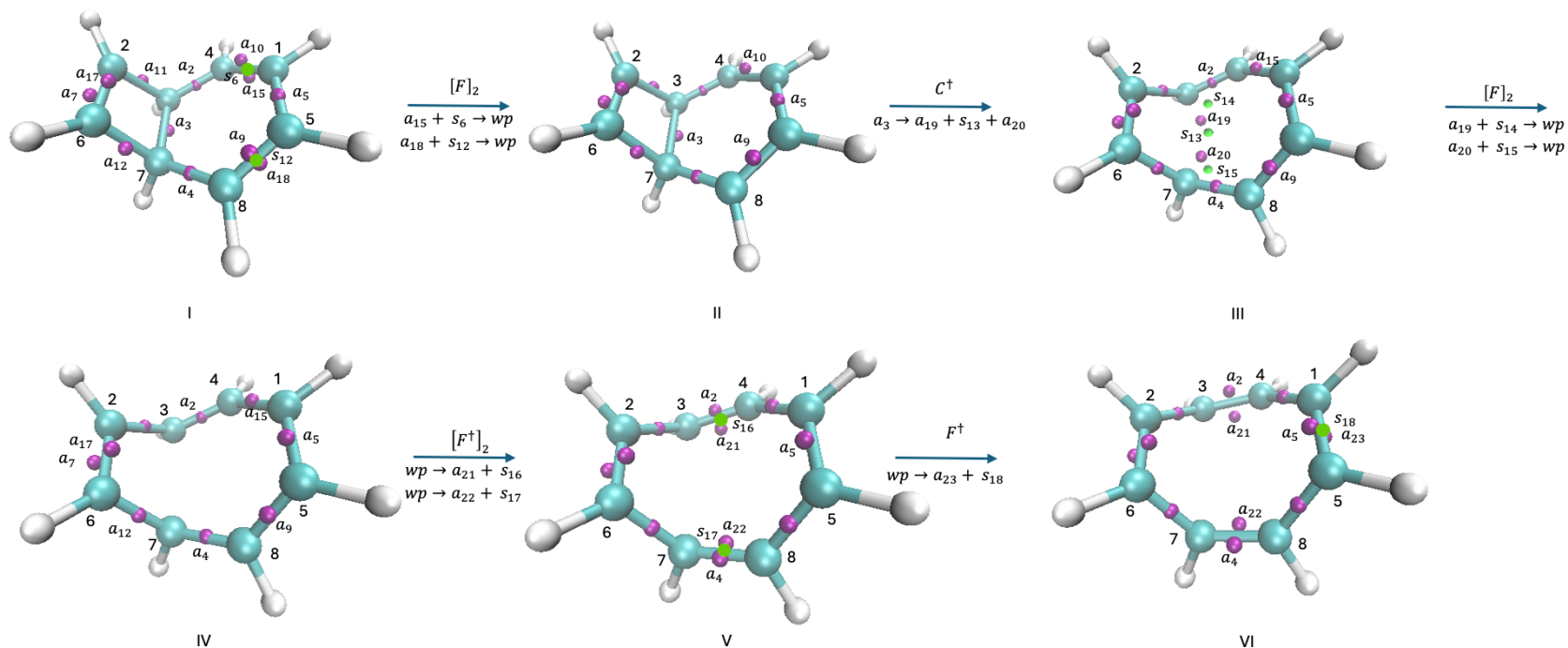
The CUB shape is highly distorted at the point where the cage opens, i.e., the C4-C8 bond breaking; thus, a plane containing a_1 and perpendicular to the C4-C8 bond fails to yield two fragments similar enough to induce any cusp flags. It is worth noting that the same argument applies to the description of the ring-opening via the C1-C2 bond breaking. As previously reported, the subsequent three changes in the phase space, i.e., $SSD\ III \rightarrow SSD\ IV \rightarrow SSD\ V \rightarrow SSD\ VI$, are characterized as folds [21] since each maximum a_{14}, a_{13}, and a_6 collides each with one-index saddle CP, annihilating through $a_{14} + s_3 \rightarrow wp$, $a_{13} + s_4 \rightarrow wp$, and $a_6 + s_5 \rightarrow wp$ processes, respectively. After the C1-C4 bond length becomes 1.357 Å, two new CPs (a_{15} and s_6) are formed near a_{10}, featuring the $SSD\ VI \rightarrow SSD\ VII$ process ($wp \rightarrow a_{15} + s_6$). Subsequently, the maximum a_{16} and the index-one saddle s_7 arise near the C5 atom after the C5-C6 bond reaches the critical length of 1.792 Å, i.e., $SSD\ VII \rightarrow SSD\ VIII$ ($wp \rightarrow a_{16} + s_7$). The first topographical event marks the initial stage of the double bond between C1 and C4, whereas the second constitutes the onset of the C5-C6 bond breaking. Hence, the electron reorganizations leading to such processes must also be described via the fold unfolding as a_{10} and a_8 do not degenerate (see Supporting information, Fig S2). The next three bifurcations, i.e., $SSD\ VIII \rightarrow SSD\ IX \rightarrow SSD\ X \rightarrow SSD\ XI$, are verified to be of the fold type, as previously identified [21]. Near the C8 center, the ELF maximum a_1 merges with the saddle s_8 through the $a_1 + s_8 \rightarrow wp$ process. Then a_8 collides with s_9, and both points annihilate through the $a_8 + s_9 \rightarrow wp$ process. Lastly, a_{16} and s_{10} disappear via the $a_{16} + s_{10} \rightarrow wp$ event near the C5 center. The continuous contraction of the C2-C6 bond distance until it reaches the value of 1.370 Å leads to the apparition of the (a_{17}, s_{11}) pair near the maximum a_7, $wp \rightarrow a_{17} + s_{11}$. From a topological perspective, this maximum indicates the onset of the formation of a double bond between these carbon atoms, i.e., $SSD\ XI \rightarrow SSD\ XII$. The last significant change featuring the $CUB \rightarrow BOT$ reaction is the onset of the double bond formation in the C5-C8 region when it reaches the distance of 1.353 Å, through the $wp \rightarrow a_{18} + s_{12}$ topographical mechanism, i.e., $SSD\ XII \rightarrow SSD\ XIII$. These events are described in terms of the simplest Thom's unfolding in both cases since the |det H| at both a_7 and a_9 shows these CPs play no role in the bifurcations (see Supporting information, Fig S3). In conclusion, the full scrutiny [29] of the pyrolytic isomerization of cubane to bicyclo[4.2.0]octa-2,4,7-triene through the cage-opening process reveals no flag of the cusp unfolding along the IRC. These findings further exhibit the underlying correlation between electron density symmetry and unfoldings [24, 29, 30]. The spatial rearrangement of the density along the minimum energy path gives the molecule its geometric shape, which, in turn, dictates the local topographical behavior of pairing density fluxes associated with key chemical events, such as the bond-breaking and bond-forming processes. Thus, this rationale enables assigning, *a priori*, the correct unfolding to describe each relevant chemical change along a pathway by visually inspecting the system geometry near the event. Considering that the spatial configuration of the cubane is strongly distorted during all chemical changes, it is reasonable that the fold correctly characterizes the electron rearrangements featuring the $CUB \rightarrow BOT$ pyrolytic isomerization.

3.2. Further insights concerning the transannular ring-opening

In **Scheme 3,** we depict the sequence of significant changes featuring the $BOT \rightarrow COT$ isomerization. For this elementary step, an activation energy equal to 18.7 kcal/mol was experimentally estimated at 298 K [94], consistent with 18.0 kcal/mol obtained under pyrolysis conditions (503-533 K) [95]. The

absolute error between experimental and computed enthalpies at 533 K ranges from 0.0-5.7 kcal/mol, using the 6-31G+(d,p) basis set and various global hybrid long-range-corrected functionals, including B3LYP, ωB97X-D, M06-2X, and MN15-L. This indicates these methods are appropriate to estimate the barrier in the gas phase. The topographical analysis of ELF was performed at the MN15-L/6-31G+(d,p), for which an absolute error of 2.4 kcal/mol was observed. See the Supporting information for further details.

The first changes in the BOT reacting system are associated with the simultaneous reduction of the C1C4 and C5C8 double bonds to single ones. The maxima a_{15} and a_{18} are shown to collide with saddle points of index one when the CC distance is 1.369 Å. Consequently, each maximum-saddle pair annihilating through the $a_{15} + s_6 \rightarrow wp$ and $a_{18} + s_{12} \rightarrow wp$ events constitutes the initial stages of the π bond losses. Although the remaining a_9 and a_{15} are in the bonding regions, they are not involved in these chemical processes since the |det H| at such a position remains almost constant. However, as the topography change is imminent, the increase in the dropping ratio of this curvature metric at a_{15}, a_{18}, s_6, and s_{12} constitutes a strong flag of a bifurcation, signifying these CPs will degenerate (See Supporting information, Fig S4). Therefore, the density fluxes resulting in such bond reductions must be correlated to the fold, contrary to the previously reported assignment. The continuous stretching of the C3-C7 bond until the distance becomes 1.963 Å results in a_3 splitting into three hyperbolic CPs, namely, a_{19}, a_{20}, and s_{13}. This abrupt change in the ELF phase space occurs through the $a_3 \rightarrow a_{19} + s_{13} + a_{20}$ cusp-type mechanism [21]. The |det H| at these points fully supports such a classification. Indeed, a_3 degenerates because of the increasing separation between C3 and C7. Also, the symmetry in the Hessian values at the new maxima is a strong flag, evidencing the cusp nature of this chemical event [29] (see Supporting information, Fig S5). In this scenario, it is crucial to note the substantial differences between the reduction of double to single bonds and the C3-C7 homolysis regarding the characterization provided by |det H|. In the latter case, the reverse IRC traversing yields that Hessian at the three points decreases, and at the merging point, these CPs have a similar Hessian value, a direct consequence of their spatial proximity. In contrast, the |det H| picture of the former case radically differs since only two points degenerate, unveiling the underlying fold features of such electron reorganizations. The following two changes in the ELF topography co-occur as maxima a_{19} and a_{20} merge with two saddle points of index one via fold catastrophes, namely $a_{19} + s_{14} \rightarrow wp$ and $a_{20} + s_{15} \rightarrow wp$ [21]. The (a_{21}, s_{16}) and (a_{22}, s_{17}) pairs emerge simultaneously from wandering points in the C3-C4 and C7-C8 single bond regions, respectively, at a distance of 1.370 Å. These new ELF maxima mark the onset of the formation of π bonds. However, a_2 and a_4 are not involved in the chemical changes even though a_{21} and a_{22} arise in the respective localities of the former points. Therefore, fold functions should better characterize both topographical transformations [21]. The arising of a_{23} and s_{18} in the vicinity of a_5 constitutes the last change in the ELF phase space and was misassigned as a cusp-type catastrophe [21]. The determinant of the Hessian evaluated at a_5 evidence that this point is not degenerate, meaning the (a_{23}, s_{18}) pair appears through the simplest fold unfolding (see Supporting Information Fig. S6).
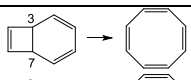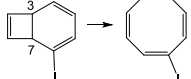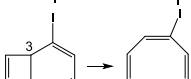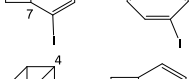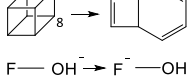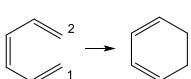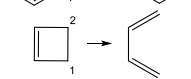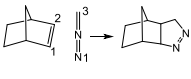
9

Scheme 3. Simplified molecular structures, critical points, and topology changes connecting the different structural stability domains (SSDs, labeled using Roman numbers), which feature bonding states associated with the $BOT \rightarrow COT$ process. Violet numbered spheres represent ELF maxima, and green numbered spheres are saddles of index one. The BOT, the transition state (TS), and the COT species belong to SSDs I, III, and VI, respectively. The labels $F^{\dagger}$ or F represent fold bifurcations that increase or decrease the number of basins, respectively, as summarized by the process below the arrow.

The formation and reduction of all double bonds featuring the $BOT \rightarrow COT$ transannular ring opening cannot be cusp catastrophes as previously assigned [21]. Flags for the cusp polynomial can be exclusively observed in just one relevant chemical event, i.e., the C3-C7 bond breaking (i.e., the transannular ring-opening process). This finding further underscores the significance of the density symmetry persistency near the topographical bifurcation [24, 29, 30, 32]. In this context, we want to stress that a perpendicular plane to the C3-C7 stretching bond containing a_3 yields two identical fragments. The symmetry persists before and after this change in the ELF phase space; thus, each fragment, specifically C3 and C7, exerts the same attracting power on the pairing density represented by a_3. Consequently, this CP degenerates and splits into three hyperbolic points. This fact is congruent with the non-polarity of this bond. The new maxima are characterized by the same statistical (e.g., electron population) and local curvature (e.g., the Hessian matrix) metrics, further supporting the balance in the electronegativity featuring the C3 and C7 centers at this reaction stage.

3.3. Chemical bond polarity and universal unfoldings

To further explore the interplay between electron density symmetry persistency, bond polarity, and unfolding flags, we have evaluated the bond polarity index [70, 71] between selected pairs of atoms for nine reacting systems (see **Table 1**).
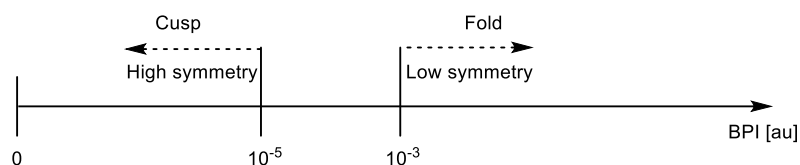
Table 1. Bond polarity index, BPI, in au for specific bonds, considering the transition state (TS) and reactant configurations for reactions in the vacuum phase. Computed, $\Delta H^{\ddagger}_{comp}$, and experimental, $\Delta H^{\ddagger}_{exp}$, activation enthalpies in kcal/mol. The activation enthalpy was calculated at $T = 298$ K when no experimental reference was available.

No.	Level of Theory	Reaction	Examined Bond	BPI$_{reactant}$	BPI$_{TS}$	$\Delta H^{\ddagger}_{comp}/\Delta H^{\ddagger}_{exp}$	ELF Catastrophe
R1	MN15-L/6-31G(d)		C3-C7	0.000	2.000×10^{-6}	19.9 /16.9(533K)[20]	Cusp
R2	MN15-L/LANL2TZ		C3-C7	4.574×10^{-3}	3.825×10^{-3}	17.7 / -	Fold
R3	MN15-L/LANL2TZ		C3-C7	7.000×10^{-6}	1.300×10^{-5}	17.7 / -	Cusp
R4	B3LYP/6-31G(d)		C4-C8	7.000×10^{-6}	3.284×10^{-2}	78.0 / -	Fold
R5	M06-2X/6-311G(2df,p)		C-F	-9.006×10^{-2}	-2.193×10^{-1}	10.2 /2.1(297K)[96]	Fold
R6	ωB97X-D/6-31G(d)		C1⋯C2	1.200×10^{-5}	-1.600×10^{-5}	21.2 /29.0(430K)[97]	Cusp
R7	ωB97X-D/6-31G(d)		C1-C2	-2.000×10^{-6}	-2.200×10^{-5}	38.5 /32.0(440K)[98-100]	Cusp
R8	MPW1K/6-31G(d,p)		C1⋯N1	-	6.280×10^{-2}	14.3 /13.2(313K)[101]	Fold
			C2⋯C3	-	3.251×10^{-2}		Fold
R9	ωB97X-D/6-31G(d)		C1⋯C3	-	9.503×10^{-3}	18.2 /24.3(800K)[102]	Fold
			C2⋯C4	-	9.496×10^{-3}		Fold

11

This set includes ubiquitous reaction classes broadly applied in organic synthesis and biochemical processes: isomerizations (R1-R4), bimolecular nucleophilic substitution (R5), and pericyclic processes, including electrocyclic (R6-R7) and cycloaddition (R8-R9) subclasses. For convenience, the isomerization mainly comprises iodine-substituted and -unsubstituted species of BOT and COT. In the case of R5, OH^- is the nucleophile, while fluorine acts as the leaving group. The cyclization of 1,3-cis-5-hexatriene (R6), the cyclobutene to 1,3-butadiene conversion (R7), the 1,3-dipolar cycloaddition between diazomethane and norbornene (R8), and the archetypal Diels-Alder reaction between 1,3-butadiene and ethylene (R9), are thermally driven processes typically rationalized using the orbital symmetry. Ethane (H_3C-CH_3), diazane (H_2N-NH_2), and molecular fluorine (F_2) served as reference systems for computing the energy index (EI) of carbon, nitrogen, and fluorine atoms, respectively.

A comprehensive overview of the bond polarity changes and ELF catastrophes for various reactions is reported in Table 1, highlighting the impact of different theoretical methods on the calculated properties. This information can be crucial for understanding the electronic changes occurring during chemical reactions and selecting appropriate computational methods for future studies. The absolute deviation between computed and experimental activation enthalpy ranges from 1.1 to 8.1 kcal/mol, indicating the reliability of the level of theory used for computing each BPI.

The analysis of bond polarity index differences and ELF catastrophes reveals significant insights into the electronic changes occurring during chemical reactions. For reactions R1 and R3, involving BOT and 2,5-diiodobicyclo[4.2.0]octa-2,4,7-triene, respectively, the BPI values for the C3-C7 bond are very small, indicating minimal changes in electron density, which is consistent across different topographical assignations and suggests a symmetrical distribution of electron density around the breaking bond. In contrast, reaction R2, involving a single substituted iodine species, shows a substantial increase in BPI by two-three orders of magnitude for the same bond, reflecting a significant reorganization of electron density and a major change in bond polarity. A low BPI value ($\sim 10^{-6}$ au) is observed for C4-C8 in CUB (R4), reflecting its highly symmetrical structure; however, this value increases by four orders of magnitude upon reaching the transition state, highlighting pronounced disparities in electron density distribution and underscoring the critical role of density symmetry near topographical bifurcations. Correspondingly, a fold catastrophe is observed, as discussed above. For the prototypical Diels-Alder reaction (R9) between 1,3-butadiene and ethylene, the relatively high BPI value strongly supports the fold [24, 32] classification over the cusp [64, 103] concerning the electron reorganizations featuring the ring closure, indicating significant changes in electron density and bond polarity. These observations underscore the possibility of integrating both fold and cusp polynomials into a unified model for scaling the bond polarity index, where the fold function describes a larger interval of BPI values suitable for bond-forming and bond-breaking processes with low electron density symmetry. In contrast, the cusp function characterizes exceptional cases of high-density symmetry. Such a fold-cusp composite model comprising universal functions (See Scheme 4) provides a robust framework for understanding the chemical bond polarity along reactive coordinates, offering valuable insights into various chemical systems' electronic structure and reactivity.

Scheme 4. High absolute BPI values ($\geq \sim 10^{-3}$ au) featuring the catastrophic region (e.g., the TS configuration) correlate with the fold unfolding, which characterizes bond-forming and bond-breaking processes exhibiting a low symmetry of electron density. In contrast, such phase spaces with low BPI ($\leq \sim 10^{-5}$ au) constitute a cusp flag, which describes relevant electron reorganizations showing a high-density symmetry relative to a plane perpendicular to the breaking/forming bond.

4. Concluding remarks

The criteria for assigning electron rearrangements along the intrinsic reaction coordinate that leads to bond formation and breaking processes during the pyrolytic isomerization of cubane (CUB) to 1,3,5,7-cyclooctatetraene (COT) have been meticulously examined from both thermochemical and bonding perspectives. Our study applied a recently developed methodology [29] that adheres to the foundational principles of bonding evolution theory (BET) [22]. The computed gas-phase activation enthalpies using state-of-the-art DFT functionals align well with experimental values. Notably, no indication of a cusp-type function was detected during the initial step of the reaction mechanism, specifically the thermal conversion of CUB to bicyclo[4.2.0]octa-2,4,7-triene (BOT). This conclusion was drawn by examining the modulus of the Hessian determinant at all potentially degenerate critical points (CPs) and their relative distances. Contrary to previous reports [21], all relevant fluxes of the pairing density must be described in terms of fold unfolding. The transannular ring opening in the second step is particularly significant, as it allows for visualizing characteristics indicative of a cusp-type catastrophe, facilitating a direct comparison with fold features. This finding underscores the importance of density symmetry persistence near topographical events, which plays a crucial role in determining the type of bifurcation. The fulfillment of this condition serves as a reliable descriptor for assigning the unfolding a priori, based on a visual assessment of molecular geometry. This fact reveals an intricate correlation between key electron density fluxes, the most stable molecular configuration, and the local topographical description of significant chemical changes. Consequently, it establishes a direct link between topology and the energetic features.

A fold-cusp unified model for scaling the polarity of chemical bonds is proposed by gauging such a multi-correlation. The integration of ubiquitous reaction classes into the analysis, including isomerization, bimolecular nucleophilic substitution, and cycloaddition, showed that values of the BPI within the interval $[0, 10^{-5}]$ au correlate with the cusp unfolding, whereas the fold spans over a broader spectrum, $[10^{-3}, \infty)$ au. These insights stress that *the cusp is the adequate polynomial to describe chemical processes when a plane perpendicular to the breaking/forming bond yields two equivalent molecular moieties*, and since this unfolding involves three CPs. Bond cleavage aligns with chemists' expectations due to the formation of new densities near reacting centers, exemplified in homolytic bond breakings. Consequently, the *fold is expected to characterize most chemical events since no particular condition is required*. This fact is corroborated by the $CUB \rightarrow COT$ stepwise reaction mechanism and accurately captured by the elucidated unified model. Using the standard proposed notation [23], and strongly contrasting with previous reports [21], the adequate sequence of catastrophes describing the changes of the ELF topology along the IRC for the complete $CUB \rightarrow BOT \rightarrow COT$ is η-1-13-F†F†FFFF†F†FFFF†F†-2-6-[F]$_2$C†[F]$_2$[F†]$_2$F†-0. These findings emphasize the

13

importance of rigorously applying Bonding Evolution Theory (BET), particularly in accurately identifying the unfoldings that describe key electron rearrangements [24-29, 31-35, 104, 105].

Acknowledgments

Supporting Information

1. Figure S1. Variation in the modulus of the Hessian determinant, |det H|, at a1 (Panel a) and at a2 (Panel b) along the IRC for the process CUB→ BOT.
2. Figure S2. Variation in the modulus of the Hessian determinant, |det H|, at a10 (Panel a) and at a8 (Panel b) along the IRC for the process CUB→ BOT.
3. Figure S3. Variation in the modulus of the Hessian determinant, |det H|, at a7 (Panel a) and at a9 (Panel b) along the IRC for the process CUB→ BOT.
4. Figure S4. Variation in the modulus of the Hessian determinant, |det H|, at CPs a10, a15, and s6 (Panel a) and at points a9, a18, and s12 (Panel b) along the IRC for the process BOT→COT.
5. Figure S5. Variation in the modulus of the Hessian determinant, |det H|, at points a3, a19, a20, and s13 as we move along the IRC for the process BOT→COT.
6. Figure S6. Variation in the modulus of the Hessian determinant, |det H|, at points a2 (Panel a), a4 (Panel b), and a5 (Panel c) when we traverse the IRC for the process BOT→COT.
7. Optimized cartesian coordinates for minima and the first-order saddle point (TS) featuring the pyrolytic isomerization of cubane to bicyclo[4.2.0]octa-2,4,7-triene at the B3LYP/6-31G(d), and B3LYP/6-31+G(d,p) DFT levels.
8. Optimized Cartesian coordinates for minima and the first-order saddle point (TS) featuring the pyrolytic isomerization of bicyclo[4.2.0]octa-2,4,7-triene to 1,3,5,7-cyclooctatetraene at the B3LYP/6-31+G(d,p), ωB97X-D/6-31+G(d,p), M06-2X/6-31+G(d,p), and MN15-L/6-31+G(d,p) DFT levels.
9. Optimized Cartesian coordinates for minima and the first-order saddle point (TS) of reactions R1-R9.
10. Optimized Cartesian coordinates of reference species used for computing the bond polarity index (BPI).
11. Table S1. Performance of DFT levels in predicting the activation enthalpy of the thermal isomerization of bicyclo[4.2.0]octa-2,4,7-triene to 1,3,5,7-cyclooctatetraene at 533 K.

Author Information

Corresponding Authors

*Leandro Ayarde-Henríquez – Trinity College Dublin. School of Physics, Dublin 2, Ireland. AMBER, Advanced Materials and BioEngineering Research Centre, Dublin 2, D02 CP49, Ireland. E–mail: leandro.ayarde@tcd.ie ORCID ID: https://orcid.org/0000–0001–5963–6028.

*Cristian Guerra – Universidad Autónoma de Chile. Facultad de Ingeniería. Avenida Pedro de Valdivia 425, 7500912, Santiago de Chile. Chile; Universidad de Córdoba. Grupo de Química Computacional. Facultad de Ciencias Básicas. Carrera 6 No. 77-305, Montería-Córdoba, Colombia. E-mail: xguerracbn@gmail.com. ORCID ID: https://orcid.org/0000-0002-9664-2504.

*Eduardo Chamorro – Universidad SEK Chile. Instituto de Investigación Interdisciplinar en Ciencias Biomédicas (I3CBSEK). Santa María 0760, Providencia, Santiago, Chile. E-mail: ed.chamorro9@gmail.com. ORCID ID: https://orcid.org/0000-0002-9200-9859.

Author Contributions

L. A.-H. and E.C: project supervision, conceptualization, data analysis, and manuscript writing; L. A.-H. and C. G.: calculations, reaction paths, and characterization; L. A.-H. and E. C.: data analysis and calculations. All authors reviewed and commented on the manuscript.

Conflicts of interest

There are no conflicts to declare.

15

References

[1] Biegasiewicz KF, Griffiths JR, Savage GP, Tsanaktsidis J, Priefer R (2015) Cubane: 50 Years Later. Chem. Rev. 115: 6719-6745. 10.1021/cr500523x

[2] Chalmers BA, Xing H, Houston S, Clark C, Ghassabian S, Kuo A, Cao B, Reitsma A, Murray CEP, Stok JE, Boyle GM, Pierce CJ, Littler SW, Winkler DA, Bernhardt PV, Pasay C, De Voss JJ, McCarthy J, Parsons PG, Walter GH, Smith MT, Cooper HM, Nilsson SK, Tsanaktsidis J, Savage GP, Williams CM (2016) Validating Eaton's Hypothesis: Cubane as a Benzene Bioisostere. Angew. Chem.-Int. Edit. 55: 3380-3385. 10.1002/anie.201510675

[3] Reekie TA, Williams CM, Rendina LM, Kassiou M (2019) Cubanes in Medicinal Chemistry. J. Med. Chem. 62: 1078-1095. 10.1021/acs.jmedchem.8b00888

[4] Mykhailiuk PK (2019) Saturated bioisosteres of benzene: where to go next? Org. Biomol. Chem. 17: 2839-2849. 10.1039/c8ob02812e

[5] Nagasawa S, Iwabuchi Y (2024) Recent Progress in Accessing Multi-functionalized Caged Hydrocarbons: En Route to Highly Functionalized Saturated (Bio)isosteres of Benzene Rings. Synthesis 18. 10.1055/a-2360-8218

[6] Tsien J, Hu C, Merchant RR, Qin T (2024) Three-dimensional saturated C(sp^3)-rich bioisosteres for benzene. Nat. Rev. Chem. 23. 10.1038/s41570-024-00623-0

[7] He Y, Liu Y, Zheng HJ, Xiang Z, Zhou Z, Geng FT, Geng LL, Dikarev EV, Han HX (2024) From cubane-assembled Mn-oxo clusters to monodispersed manganese oxide colloidal nanocrystals. Chem. Sci. 15: 12. 10.1039/d4sc01451k

[8] Li H, Gao YL, Ma JJ (2022) Advances in nonclassical phenyl bioisosteres for drug structural optimization. Future Med. Chem. 14: 1681-1692. 10.4155/fmc-2022-0188

[9] Li JB, Stein R, Adrion DM, Lopez SA (2021) Machine-Learning Photodynamics Simulations Uncover the Role of Substituent Effects on the Photochemical Formation of Cubanes. J. Am. Chem. Soc. 143: 20166-20175. 10.1021/jacs.1c07725

[10] Chen C, Liu DY, Deng SY, Zhong LX, Chan SHY, Li SZ, Hng HH (2021) Accurate machine learning models based on small dataset of energetic materials through spatial matrix featurization methods. J. Energy Chem. 63: 364-375. 10.1016/j.jechem.2021.08.031

[11] Eaton PE (1992) CUBANES - STARTING MATERIALS FOR THE CHEMISTRY OF THE 1990S AND THE NEW CENTURY. Angew. Chem.-Int. Edit. Engl. 31: 1421-1436. 10.1002/anie.199214211

[12] Wiesenfeldt MP, Rossi-Ashton JA, Perry IB, Diesel J, Garry OL, Bartels F, Coote SC, Ma XS, Yeung CS, Bennett DJ, MacMillan DWC (2023) General access to cubanes as benzene bioisosteres. Nature 618: 513-+. 10.1038/s41586-023-06021-8

[13] Radhoff N, Daniliuc CG, Studer A (2023) Lewis Acid Catalyzed Formal (3+2)-Cycloaddition of Bicyclo 1.1.0 butanes with Ketenes. Angew. Chem.-Int. Edit. 62: 6. 10.1002/anie.202304771

[14] Fujiwara K, Nagasawa S, Maeyama R, Segawa R, Hirasawa N, Hirokawa T, Iwabuchi Y (2024) Biological Evaluation of Isosteric Applicability of 1,3-Substituted Cuneanes as *m*-Substituted Benzenes Enabled by Selective Isomerization of 1,4-Substituted Cubanes. Chem.-Eur. J. 30: 6. 10.1002/chem.202303548

[15] Doedens RJ, Eaton PE, Fleischer EB (2017) The Bent Bonds of Cubane. Eur. J. Org. Chem. 2017: 2627-2630. 10.1002/ejoc.201700427

[16] Takebe H, Matsubara S (2024) Decoration on Cubane with an Awareness of Chirality: Development of Substituted Cubane Syntheses. Synthesis 56: 16-28. 10.1055/a-2124-3823

[17] Haase F, Lotsch BV (2020) Solving the COF trilemma: towards crystalline, stable and functional covalent organic frameworks. Chem. Soc. Rev. 49: 8469-8500. 10.1039/d0cs01027h

[18] Eaton PE, Zhang MX, Gilardi R, Gelber N, Iyer S, Surapaneni R (2002) Octanitrocubane: A new nitrocarbon. Propellants Explos. Pyrotech. 27: 1-6.

[19] Khakimov DV, Svitanko IV, Pivina TS (2024) Computational insight into the crystal structures of cubane and azacubanes. J. Mol. Model. 30: 9. 10.1007/s00894-024-05891-7

[20] Martin HD, Urbanek T, Pfohler P, Walsh R (1985) THERMAL-BEHAVIOR OF C8H8 HYDROCARBONS AND SMALL AND MEDIUM RINGS - THE PYROLYSIS OF CUBANE - AN EXAMPLE OF A THERMALLY INDUCED HOT MOLECULE REACTION. J. Chem. Soc.-Chem. Commun. 964-965. 10.1039/c39850000964

[21] Seif A, Domingo LR, Zahedi E, Ahmadi TS, Mazarei E (2020) Unraveling the kinetics and molecular mechanism of gas phase pyrolysis of cubane to 8 annulene. RSC Adv. 10: 32730-32739. 10.1039/d0ra05371f

[22] Krokidis X, Noury S, Silvi B (1997) Characterization of elementary chemical processes by catastrophe theory. Journal of Physical Chemistry A 101: 7277-7282. 10.1021/jp9711508

[23] Berski S, Andres J, Silvi B, Domingo LR (2006) New findings on the Diels-Alder reactions. An analysis based on the bonding evolution theory. J Phys. Chem. A 110: 13939-13947. 10.1021/jp068071t

[24] Ayarde-Henríquez L, Guerra C, Duque-Noreña M, Rincón E, Pérez P, Chamorro E (2021) Are There Only Fold Catastrophes in the Diels-Alder Reaction Between Ethylene and 1,3-Butadiene? J. Phys. Chem. A 125: 5152-5165. 10.1021/acs.jpca.1c01448

[25] Guerra C, Ayarde-Henríquez L, Rodríguez-Núñez YA, Ensuncho A, Chamorro E (2023) Elucidating the N-N and C-N Bond-breaking Mechanism in the Photoinduced Formation of Nitrile Imine. ChemPhysChem 24: 7. 10.1002/cphc.202200867

[26] Guerra C, Ayarde-Henríquez L, Rodriguez-Nuñez YA, Chamorro E, Ensuncho AE (2023) Mechanistic insights into benzyne formation via 1,2-di-iodobenzene photolysis. New J. Chem. 47: 21270-21275. 10.1039/d3nj04022d

[27] Guerra C, Ayarde-Henríquez L, Chamorro E, Ensuncho A (2023) Uncovering Triradicaloid Structures in S_1 Benzene Photochemistry. ChemPhotoChem 7: 12. 10.1002/cptc.202200263

[28] Ayarde-Henríquez L, Guerra C, Duque-Noreña M, Chamorro E (2023) A simple topology-based model for predicting the activation barriers of reactive processes at 0 K. Phys. Chem. Chem. Phys. 25: 14274-14284. 10.1039/d3cp01008b

[29] Ayarde-Henriquez L, Guerra C, Duque-Noreña M, Chamorro E (2023) Revisiting the bonding evolution theory: a fresh perspective on the ammonia pyramidal inversion and bond dissociations in ethane and borazane. Phys. Chem. Chem. Phys. 25: 27394-27408. 10.1039/d3cp03572g

[30] Guerra C, Ayarde-Henríquez L, Duque-Noreña M, Chamorro E (2022) On Electron Pair Rearrangements in Photochemical Reactions: 1,3-Cyclohexadiene Ring Opening. J. Phys. Chem. A 126: 395-405. 10.1021/acs.jpca.1c07800

[31] Guerra C, Ayarde-Henríquez L, Duque-Noreña M, Chamorro E (2022) Photochemically Induced 1,3-Butadiene Ring-Closure from the Topological Analysis of the Electron Localization Function Viewpoint. ChemPhysChem 23: 9. 10.1002/cphc.202200217

[32] Ayarde-Henríquez L, Guerra C, Duque-Noreña M, Rincón E, Pérez P, Chamorro E (2022) On the Notation of Catastrophes in the Framework of Bonding Evolution Theory: Case of Normal and Inverse Electron Demand Diels-Alder Reactions. ChemPhysChem 23: 6. 10.1002/cphc.202200343

[33] Ayarde-Henríquez L, Guerra C, Duque-Noreña M, Chamorro E (2022) Unraveling the role of the electron-pair density symmetry in reaction mechanism patterns: the Newman-Kwart rearrangement. New J. Chem. 46: 12002-12009. 10.1039/d2nj01501c

[34] Guerra C, Ayarde-Henríquez L, Duque-Noreña M, Chamorro E (2021) Unraveling the Bonding Nature Along the Photochemically Activated Paterno-Buchi Reaction Mechanism. ChemPhysChem 22: 2342-2351. 10.1002/cphc.202100594

[35] Guerra C, Ayarde-Henríquez L, Duque-Noreña M, Cárdenas C, Pérez P, Chamorro E (2021) On the nature of bonding in the photochemical addition of two ethylenes: C-C bond formation in the excited state? Phys. Chem. Chem. Phys. 23: 20598-20606. 10.1039/d1cp03554a

[36] Becke AD, Edgecombe KE (1990) A Simple Measure of Electron Localization in Atomic and Molecular Systems. J. Chem. Phys. 92: 5397-5403. 10.1063/1.458517

[37] Arnold VI, Afrajmovich VS, Ol'yashenko YS, Shil'nikov LP (1999) Bifurcation Theory and Catastrophe Theory. Springer-Verlag, Berlin-Heildelberg, Germany.

[38] Thom R (1972) Structural stability and morphogenesis: An outline of a general theory of models. Westview Press.

[39] Gilmore R (1993) Catastrophe Theory for Scientists and Engineers Dover Publications.

[40] Poston T, Stewart I (1978) Catastrophe Theory and Its Applications. Pitman Publishin Limited, London. San Francisco. Melbourne.

[41] Bader RFW (1994) Atoms in Molecules. A Quantum Theory. Oxford University Press Inc., New York, USA.

[42] Robinson C (1999) Dynamical Systems: Stability, Symbolic Dynamics, and Chaos. CRC-Press.

[43] Castrigiano DPL, Hayes SA (2018) Catastrophe Theory. Second Edition ed., CRC Press. Taylor & Francis Group. , Boca Raton, FL 33487-2742.

[44] Savin A, Nesper R, Wengert S, Fassler TF (1997) ELF: The electron localization function. Angew. Chem.-Int. Edit. 36: 1809-1832.

[45] Savin A (2005) On the significance of ELF basins. Journal of Chemical Sciences 117: 473-475. 10.1007/bf02708351

[46] Savin A (2005) The electron localization function (ELF) and its relatives: interpretations and difficulties. Journal of Molecular Structure-Theochem 727: 127-131. 10.1016/j.theochem.2005.02.034

[47] Domingo LR, Chamorro E, Perez P (2010) Understanding the mechanism of non-polar Diels-Alder reactions. A comparative ELF analysis of concerted and stepwise diradical mechanisms. Org. Biomol. Chem. 8: 5495-5504. 10.1039/c0ob00563k

[48] Pilme J, Renault E, Ayed T, Montavon G, Galland N (2012) Introducing the ELF Topological Analysis in the Field of Quasirelativistic Quantum Calculations. J. Chem. Theory Comput. 8: 2985-2990. 10.1021/ct300558k

[49] Causa M, D'Amore M, Garzillo C, Gentile FS, Savin A (2013) The Bond Analysis Techniques (ELF and Maximum Probability Domains) Application to a Family of Models Relevant to Bio-Inorganic Chemistry, in: M.V. Putz, D.M.P. Mingos (Eds.), Applications of Density Functional Theory to Biological and Bioinorganic Chemistry pp. 119-141.

[50] Grin Y, Savin A, Silvi B (2014) The ELF perspective of chemical bonding, in: G. Frenking, S. Shaik (Eds.), The Chemical Bond: Fundamentals and Models, Wiley-VCH Verlag GmbH & Co. KGaApp. 345-382.

[51] Ayers PLa, Boyd RJb, Bultinck P, Caffarel Md, Carbo-Dorca Re, Causa Mf, Cioslowski Jg, Contreras-Garcia Jh, Cooper DLi, Coppens Pj, Gatti Ck, Grabowsky Sl, Lazzeretti Pm, Macchi Pn, Martin Pendas Ao, Popelier PLAp, Ruedenberg Kr, Rzepa Hs, Savin Ah, Sax At, Schwarz WHEu, Shahbazian Sw, Silvi Bh, Sola Me, Tsirelson Vx (2015) Six questions on topology in theoretical chemistry. Comput. Theor. Chem. 1053: 2-16. 10.1016/j.comptc.2014.09.028

[52] Silvi B, Savin A (1994) Classification of Chemical-Bonds Based on Topological Analysis of Electron Localization Functions. Nature 371: 683-686. 10.1038/371683a0

[53] Savin A, Silvi B, Colonna F (1996) Topological analysis of the electron localization function applied to delocalized bonds. Can. J. Chem. 74: 1088-1096. 10.1139/v96-122

[54] Silvi B (2002) The synaptic order: a key concept to understand multicenter bonding. Journal of Molecular Structure 614: 3-10. 10.1016/s0022-2860(02)00231-4

[55] Savin A, Becke AD, Flad J, Nesper R, Preuss H, Vonschnering HG (1991) A New Look at Electron Localization. Angew. Chem.-Int. Edit. 30: 409-412. 10.1002/anie.199104091

[56] Matito E, Silvi B, Duran M, Sola M (2006) Electron localization function at the correlated level. J. Chem. Phys. 125: 024301. 10.1063/1.2210473

[57] Ponec R, Chaves J (2005) Electron pairing and chemical bonds. Electron fluctuation and pair localization in ELF domains. J. Comput. Chem. 26: 1205-1213. 10.1002/jcc.20257

[58] Ayers PW (2005) Electron localization functions and local measures of the covariance. J. Chem. Sci. 117: 441-454. 10.1007/bf02708348

[59] Thom R (1994) Structural Stability and Morphogenesis: An Outline of a General Theory of Models. Westview Press (January 21, 1994), London-Amsterdam.

[60] Zeeman EC (1976) CATASTROPHE THEORY. Sci.Am. 234: 65-&. 10.1038/scientificamerican0476-65

[61] Woodcock AER, Poston A (1974) Geometrical Study of Elementary Catastrophes,. Springer-Verlag Berlin Heidelberg, Berlin.

[62] Domingo LR, Rios-Gutierrez M, Perez P, Chamorro E (2016) Understanding the 2n+2n reaction mechanism between a carbenoid intermediate and CO2. Mol. Phys. 114: 1374-1391. 10.1080/00268976.2016.1142127

[63] Berski S, Andres J, Silvi B, Domingo LR (2003) The joint use of catastrophe theory and electron localization function to characterize molecular mechanisms. A density functional study of the Diels-Alder reaction between ethylene and 1,3-butadiene. J. Phys. Chem. A 107: 6014-6024. 10.1021/jp030272z

[64] Polo V, Andres J, Berskit S, Domingo LR, Silvi B (2008) Understanding reaction mechanisms in organic chemistry from catastrophe theory applied to the electron localization function topology. J. Phys. Chem. A 112: 7128-7136. 10.1021/jp801429m

[65] Berski S, Ciunik LZ (2015) The mechanism of the formation of the hemiaminal and Schiff base from the benzaldehyde and triazole studied by means of the topological analysis of electron localisation function and catastrophe theory. Mol. Phys. 113: 765-781. 10.1080/00268976.2014.974702

[66] Cmikiewicz A, Gordon AJ, Berski S (2018) Characterisation of the reaction mechanism between ammonia and formaldehyde from the topological analysis of ELF and catastrophe theory perspective. Struct. Chem. 29: 243-255. 10.1007/s11224-017-1024-x

[67] Chamorro E, Guerra C, Henríquez L, Duque M, Pérez P, Rincón E (2023) New insights from a bonding evolution theory based on the topological analysis of the electron localization function, pp. 465-481.

[68] Allred AL (1961) Electronegativity values from thermochemical data. J. Inorg. Nucl. Chem. 17: 215-221. 10.1016/0022-1902(61)80142-5

[69] Tantardini C, Oganov AR (2021) Thermochemical electronegativities of the elements. Nat. Commun. 12: 2087. 10.1038/s41467-021-22429-0

[70] Allen LC, Egolf DA, Knight ET, Liang CX (1990) BOND POLARITY INDEX. J. Phys. Chem. 94: 5602-5607. 10.1021/j100377a037

[71] Reed LH, Allen LC (1992) BOND POLARITY INDEX - APPLICATION TO GROUP ELECTRONEGATIVITY. J. Phys. Chem. 96: 157-164. 10.1021/j100180a032

[72] Schlegel HB (1982) Optimization of Equilibrium Geometries and Transition Structures. J. Comput. Chem. 3: 214-218. 10.1002/jcc.540030212

[73] Schlegel HB (1995) Geometry Optimization on Potential Energy Surfaces, in: D.R. Ryarkony (ed.), Modern Electronic Structure Theory, World Scientific Publishing.

[74] Gonzalez C, Schlegel HB (1990) Reaction-Path Following in Mass-Weighted Internal Coordinates. J. Phys. Chem. 94: 5523-5527. 10.1021/j100377a021

[75] Gonzalez C, Schlegel HB (1991) Improved Algorithms for Reaction-Path Following - Higher-Order Implicit Algorithms. J. Chem. Phys. 95: 5853-5860. 10.1063/1.461606

[76] Frisch MJ, Trucks GW, Schlegel HB, Scuseria GE, Robb MA, Cheeseman JR, Scalmani G, Barone V, Mennucci B, Petersson GA, Nakatsuji H, Li X, Caricato M, Marenich AV, Bloino J, Janesko BG, Gomperts R, Mennucci B, Hratchian HP, Ortiz JV, Izmaylov AF, Sonnenberg JL, Williams-Young D, Ding F, Lipparini F, Egidi F, Goings J, Peng B, petrone A, Henderson T, Ranasinhe D, Zakrzewski VG, Gao J, Rega N, Zheng G, Liang W, Hada M, Ehara M, Toyota K, Fukuda R, Hasegawa J, Ishida M, Nakajima T, Honda Y, Kitao O, Nakai H, Vreven T, Throssell K, Montgomery Jr. JA, Peralta JE, Ogliaro F, Bearpark M, Heyd JJ, Brothers EN, Kudin KN, Staroverov VN, Keith

TA, Kobayashi R, Normand J, Raghavachari K, Rendell A, Burant JC, Iyengar SS, Tomasi J, Cossi M, Millam JM, Klene M, Adamo C, Cammi R, Ochterski JW, Martin RL, Morokuma K, Farkas Ö, Foresman JB, Fox DJ, Gaussian 16, Gaussian, Inc., Wallingford, CT, 2017.

[77] Hratchian HP, Schlegel HB (2005) Chapter 10. Finding Minima, Transition States, and Following Reaction Pathways on Ab Initio Potential Energy Surfaces, in: C.E. Dykstra, G. Frenking, K.S. Kim, G. Scuseria (Eds.), Theory and Applications of Computational Chemistry: The First 40 Years, Elsevier, Amsterdam.

[78] Fukui K (1981) The Path of Chemical-Reactions - The IRC Approach. Acc. Chem. Res. 14: 363-368. 10.1021/ar00072a001

[79] Lu T, Chen F (2012) Multiwfn: A multifunctional wavefunction analyzer. J. Comput. Chem. 33: 580-592. 10.1002/jcc.22885

[80] Humphrey W, Dalke A, Schulten K (1996) VMD - Visual molecular dynamics. J. Mol. Graph. 14: 33-38. 10.1016/0263-7855(96)00018-5

[81] Andres J, Gonzalez-Navarrete P, Sixte Safont V (2014) Unraveling Reaction Mechanisms by Means of Quantum Chemical Topology Analysis. Int. J. Quantum Chem. 114: 1239-1252. 10.1002/qua.24665

[82] Andres J, Berski S, Domingo LR, Polo V, Silvi B (2011) Describing the Molecular Mechanism of Organic Reactions by Using Topological Analysis of Electronic Localization Function. Current Organic Chemistry 15: 3566-3575. 10.2174/138527211797636156

[83] Andres J, Gracia L, Gonzalez-Navarrete P, Safont VS (2015) Chemical structure and reactivity by means of quantum chemical topology analysis. Computational and Theoretical Chemistry 1053: 17-30. 10.1016/j.comptc.2014.10.010

[84] Krokidis X, Vuilleumier R, Borgis D, Silvi B (1999) A topological analysis of the proton transfer in H5O2+. Mol. Phys. 96: 265-273. 10.1080/002689799165891

[85] Allen LC (1992) CHEMICAL INTERPRETATION - BASIS SET USE AND THE PERIODIC-TABLE. Can. J. Chem. 70: 631-635. 10.1139/v92-086

[86] Allen LC (1989) ELECTRONEGATIVITY IS THE AVERAGE ONE-ELECTRON ENERGY OF THE VALENCE-SHELL ELECTRONS IN GROUND-STATE FREE ATOMS. J. Am. Chem. Soc. 111: 9003-9014. 10.1021/ja00207a003

[87] Zhou RP, Fan SX, Fang LL, Chu BF, Zhu J (2023) Rh(III)-Catalyzed <i>N</i>-Amino-Directed C-H Coupling with 3-Methyleneoxetan-2-ones for 1,2-Dihydroquinoline-3-carboxylic Acid Synthesis. Org. Lett. 25: 8688-8692. 10.1021/acs.orglett.3c03610

[88] Menia D, Pittracher M, Kopacka H, Wurst K, Neururer FR, Leitner D, Hohloch S, Podewitz M, Bildstein B (2023) Curious Case of Cobaltocenium Carbaldehyde. Organometallics 42: 377-383. 10.1021/acs.organomet.2c00613

[89] Qian RS, Zhang YS, Zhang Y, Fu CQ, Liu C, Yang L, Liu GJ (2023) Various gas transport properties in concrete considering transporting mechanisms and testing methods-A review. Constr. Build. Mater. 389. 10.1016/j.conbuildmat.2023.131636

[90] Agapito F, Santos RC, dos Santos RMB, Simoes JAM (2015) The Thermochemistry of Cubane 50 Years after Its Synthesis: A High-Level Theoretical Study of Cubane and Its Derivatives. J. Phys. Chem. A 119: 2998-3007. 10.1021/jp511756v

[91] Pichierri F (2017) Substituent effects in cubane and hypercubane: a DFT and QTAIM study. Theor. Chem. Acc. 136: 10. 10.1007/s00214-017-2144-5

[92] Feixas F, Matito E, Duran M, Sola M, Silvi B (2010) Electron localization function at the correlated level: A natural orbital formulation. J. Chem. Theory Comput. 6: 2736-2742. 10.1021/ct1003548

[93] Matito E, Silvi B, Duran M, Sola M (2006) Electron localization function at the correlated level. J. Chem. Phys. 125. 10.1063/1.2210473

[94] Scott LT, Jones, M (1972) Rearrangements and interconversions of compounds of the formula (CH)n. Chem. Rev. 72: 181-202. 10.1021/cr60276a004

[95] Martin HD, Urbanek T, Pfohler P, Walsh R (1985) The pyrolysis of cubane; an example

of a thermally induced hot molecule reaction. J. Chem. Soc., Chem. Commun. 964-965. 10.1039/C39850000964

[96] Tanaka K, Mackay GI, Payzant JD, Bohme DK (1976) GAS-PHASE REACTIONS OF ANIONS WITH HALOGENATED METHANES AT 297+/-2 K. Can. J. Chem. 54: 1643-1659. 10.1139/v76-234

[97] Lewis KE, Steiner H (1964) 588. The kinetics and mechanism of the thermal cyclisation of hexa-1,cis-3,5-triene to cyclohexa-1,3-diene. J. Chem. Soc. (Resumed) 3080-3092. 10.1039/JR9640003080

[98] Cooper W, Walters WD (1958) The Thermal Isomerization of Cyclobutene1,2. J. Am. Chem. Soc. 80: 4220-4224. 10.1021/ja01549a025

[99] Carr RW, Jr., Walters WD (1965) The Thermal Isomerization of Cyclobutene1a. J. Phys. Chem. 69: 1073-1075. 10.1021/j100887a510

[100] Hauser WP, Walters WD (1963) THE KINETICS OF THE THERMAL ISOMERIZATION OF CYCLOBUTENE1,2. J. Phys. Chem. 67: 1328-1333. 10.1021/j100800a039

[100] Geittner J, Huisgen R, Reissig H-U (1978) Solvent Dependence of Cycloaddition Rates of Phenyldiazomethane and Activation Parameters, Heterocycles. Heterocycles 11: 109–112.

[102] Rowley D, Steiner H (1951) Kinetics of diene reactions at high temperatures. Discuss. Faraday Soc. 10: 198-213. 10.1039/DF9511000198

[103] Berski S, Andrés J, Silvi B, Domingo LR (2003) The joint use of catastrophe theory and electron localization function to characterize molecular mechanisms. A density functional study of the Diels-Alder reaction between ethylene and 1,3-butadiene. J. Phys. Chem. A 107: 6014-6024. 10.1021/jp030272z

[104] Chamorro E, Guerra C, Ayarde-Henríquez L, Duque-Noreña M, Pérez P, Rincón E, in Chemical Reactivity: Theories and Principles, eds. Kayas S, von Szentpály L, Serdaroglu G, Guo L, Elsevier, 2023, vol. 1, pp. 465-481

[105] Ayarde-Henríquez L, Guerra C, Duque-Noreña M, Pérez P, Rincón E, Chamorro E, in Electron Density: Concepts, Computation and DFT Applications, eds. Chattaraj PK, Chakraborty D, Wiley, 2024, pp. 299-312